



# Investigations of temperature effects on hydrogen diffusion and hydrogen embrittlement of X80 pipeline steel under electrochemical hydrogen charging environment

Jiaqing Li <sup>a</sup>, Ziyue Wu <sup>a</sup>, Lijie Zhu <sup>a</sup>, Zhiwu Zhang <sup>a,\*</sup>, Lin Teng <sup>a,\*</sup>, Liang Zhang <sup>b</sup>, Cheng Lu <sup>c</sup>, Rui Wang <sup>c</sup>, Che Zhang <sup>d</sup>

<sup>a</sup> College of Chemical Engineering, Fuzhou University, Fuzhou 350116, China

<sup>b</sup> International Joint Laboratory for Light Alloys (MOE), College of Materials Science and Engineering, Chongqing University, Chongqing 400044, China

<sup>c</sup> School of Mechanical, Materials, Mechatronic and Biomedical Engineering, University of Wollongong, Wollongong, NSW 2522, Australia

<sup>d</sup> Department of Mechanical Engineering, The University of Melbourne, Parkville, VIC 3010, Australia

## ARTICLE INFO

### Keywords:

Hydrogen embrittlement  
Hydrogen permeation  
Electrochemical hydrogen charging  
Embrittlement susceptibility  
Temperature effect

## ABSTRACT

The influence of temperature on hydrogen diffusion and hydrogen embrittlement of X80 steel was studied using electrochemical hydrogen charging. The hydrogen diffusion and subsurface hydrogen concentration in the steel increased with increasing the temperature. Macro slow strain rate tensile tests and microstructural analysis were performed to unveil the dependence of hydrogen-induced embrittlement susceptibility on temperature, which suggested a temperature threshold  $T_{HE, max}$  of 315 K. The demonstration of  $T_{HE, max}$  would be crucial for determining test temperatures of hydrogen-related engineering material applications.

## 1. Introduction

In the hydrocarbon processing industry, high-strength steel pipelines have emerged as essential pillars for oil and natural gas transportation. With the growing significance of hydrogen energy, blending the pressurised hydrogen into natural gas pipelines has been proposed to aspire global net zero path, aiding the de-carbonization of global greenhouse gas emissions. However, hydrogen embrittlement (HE) is a significant concern to jeopardize the structural integrity of high-strength pipeline steels [1–6], causing catastrophic accidents such as pipeline fracture, explosion and combustion. In particular, the HE susceptibility and severity will be further increased with increasing strength levels of steels [5,7,8]. Accordingly, understanding the HE susceptibility of pipeline steels is critical to their safe applications and rapid promotion of hydrogen energy.

Since the first report regarding hydrogen-induced mechanical degradation of iron and steel was published in 1875 s [9], a number of HE mechanisms have been proposed, including hydrogen-enhanced decohesion (HEDE) [10–12], hydrogen-enhanced localized plasticity (HELP) [13–15], and so on. In terms of the HEDE mechanism, it is presumed that hydrogen trapping at the crack tip decreases the cohesive

energy of atomic planes and grain boundaries (GBs), promoting cleavage-like failure. The model is hydrogen-concentration dependent, and has enormous popularity in elucidating intergranular failure when the critical hydrogen concentration in materials is reached [16]. Notwithstanding, there is a strong disagreement regarding the macroscopically observed intense slip bands and dislocation cell structures beneath the hydrogen-induced fracture surfaces [17,18]. As a plasticity-driven HE model, the HELP mechanism stems from direct environmental transmission electron microscopy (ETEM) observations of enhanced dislocation generation and mobility and dislocation pile-up in the presence of hydrogen [14,16,19], which is considered to be a prerequisite for the eventual activation of intergranular failure at specific microstructural locations [16–18]. However, there are still some opposite findings. Recently, the in-situ environmental scanning electron microscopy (ESEM) observed a very confined plastic zone nearby the crack brims, verifying the suppression of dislocation mobility due to highly concentrated hydrogen [20], contrary to the concept of the HELP model. Another experimental observation in ETEM measurements manifested that dislocations could be locked after exposure to hydrogen due to superabundant vacancies [21]. These mechanisms are not mutually exclusive and may coexist synergistically depending on the

\* Corresponding authors.

E-mail addresses: [zwzhang@fzu.edu.cn](mailto:zwzhang@fzu.edu.cn) (Z. Zhang), [tenglin@fzu.edu.cn](mailto:tenglin@fzu.edu.cn) (L. Teng).

**Table 1**

Chemical compositions of the studied X80 steel in weight percent (wt%).

Steel	C	Si	Mn	P	S	Cr	Mo	Ni	Al	Cu	Nb	Ti	V	Fe	Bal.
X80	0.05	0.21	1.82	0.007	0.001	0.012	0.18	0.033	0.035	0.012	0.07	0.012	0.007		

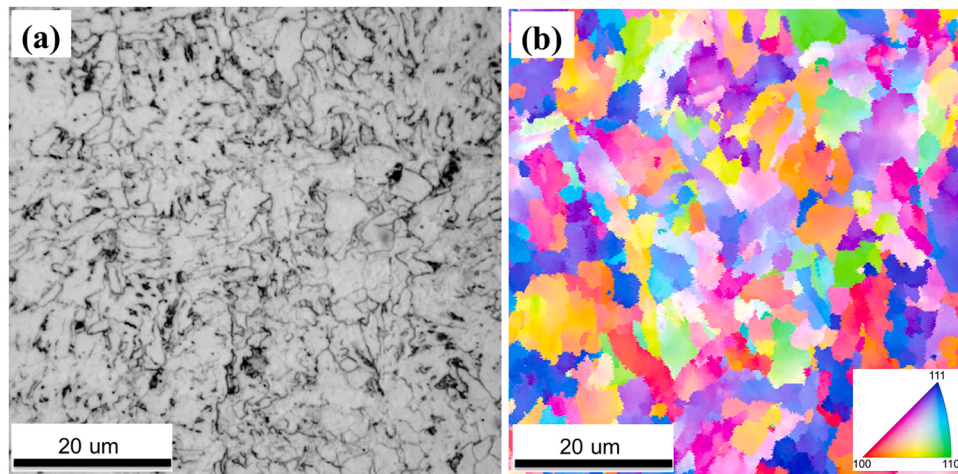


Fig. 1. Microstructures of X80 steel (a) OM image and (b) EBSD map.

experimental conditions, i.e., hydrogen charging method, mechanical loading and temperature.

Hydrogen-bearing environments in experiments are commonly established by two hydrogen charging methods: electrochemical hydrogen charging and gaseous hydrogen charging. The first method involves the immersion of specimens in acidic or alkaline solutions and employs cathodic polarization at constant current or potential to produce hydrogen atoms. By feat of this charging method, hydrogen diffusivity and trapping, hydrogen content, and hydrogen degradation effects have been intensively studied [22–24]. For instance, hydrogen permeation of several advanced high-strength steels after electrochemical charging revealed that hydrogen trapping effects were less prominent with a negative shift of potential, and hydrogen diffusion coefficient could be determined by the partial transients at the most negative potentials [25]. Further permeation experiments of three sub-sea pipeline steels under cathodic protection confirmed that the sub-surface hydrogen concentration increased with the applied cathodic polarization potential [5]. Recent in-situ/ex-situ electrochemical tensile measurements and micro-cantilever bending study by Asadiopoor et al.

[1] unveiled the dependence of mechanical behaviour of X70 pipeline steel on hydrogen charging condition; electrochemical hydrogen charging decreased yield strength, ultimate tensile strength, flow stress, and hydrogen-induced cracking.

In terms of gaseous hydrogen charging, the samples are tested and assessed under high-pressure gas-phase hydrogen environment, where the adsorption and dissociation of H<sub>2</sub> molecules generates hydrogen atoms. Using such a method, researchers have illuminated the hydrogen trapping and diffusion [26,27], fatigue crack propagation and growth [28,29], tensile-ductility loss and embrittlement features [27,30]. Note that until now, no standard test method for gaseous hydrogen charging has been established, as the kinetic laws of the dissociation of H<sub>2</sub> molecules into hydrogen atoms have not been developed. In addition, the influence of surface state of pipeline steels on the generation of hydrogen atoms is still unclear. These aspects cast doubt on the study of HE phenomenon by gaseous hydrogen charging.

There is a strong dependence of hydrogen degradation effects on the temperature for various types of structural materials such as austenitic stainless steels [31,32], nickel superalloys [33,34], and carbon steels

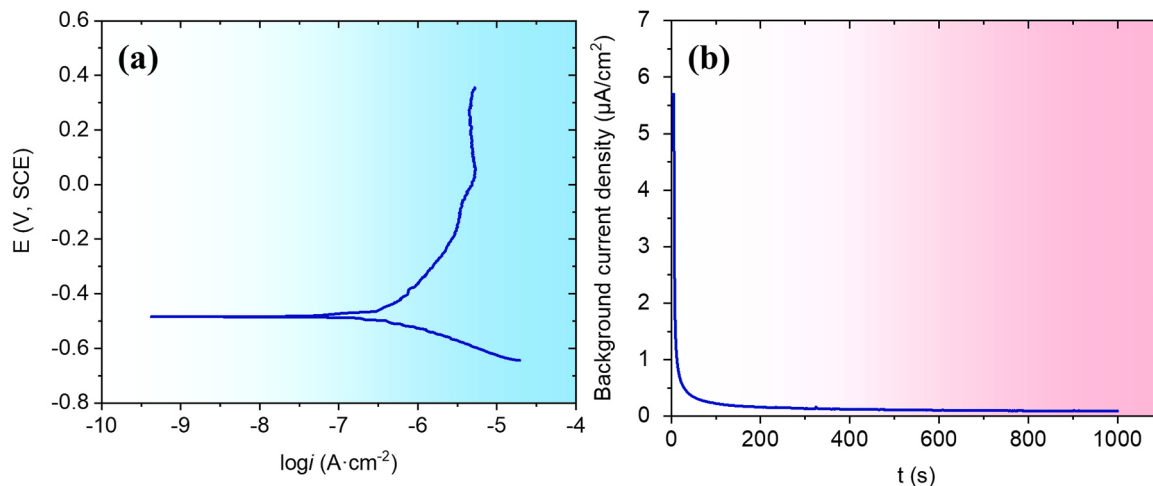


Fig. 2. (a) Potentiodynamic polarization curve of Ni-plated layer of the sample in NaOH solution, and (b) Background current density as a function of time.

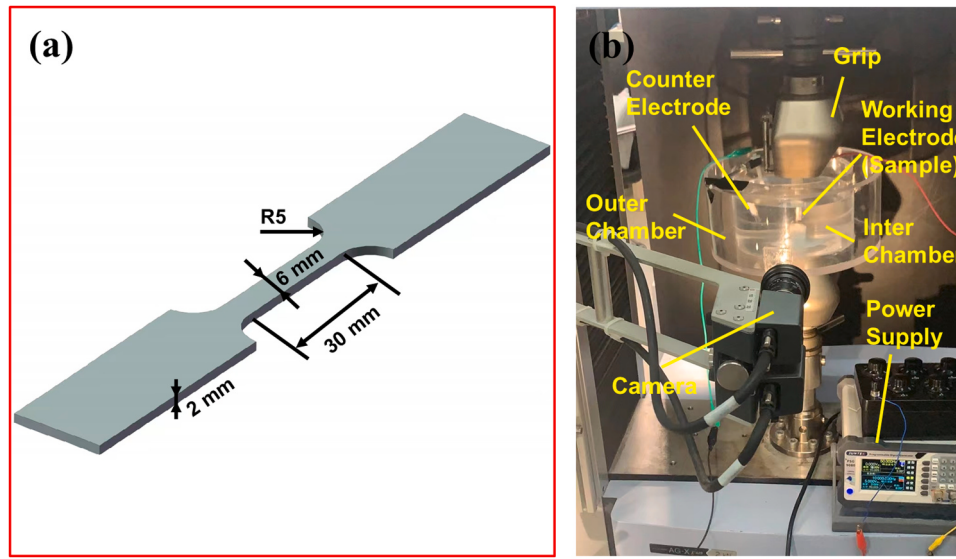


Fig. 3. (a) Dimensions of tensile samples, and (b) Set up of SSRT tests.

[35,36]. A typical curve plotting hydrogen-induced mechanical degradation versus temperature gives rise to a specific temperature  $T_{HE, max}$ , where the embrittlement susceptibility peaks. Considering various structural materials,  $T_{HE, max}$  values in the regime of about 200–340 K are generally reported using tensile tests [37]. For example, a tensile relative reduction of area measured at a tensile strain rate of  $6.7 \times 10^{-5} \text{ s}^{-1}$  in 115 MPa hydrogen gas atmosphere determined  $T_{HE, max}$  of SCM435 steel as < 230 K [36];  $T_{HE, max}$  of X90 steel was reported to be 313 K based on slow strain rate tensile (SSRT) tests in electrochemically hydrogen-precharged specimens [38]. The scenarios behind  $T_{HE, max}$  seem very complicated as the temperature effect can be found in each part of “hydrogen reaction chain” (hydrogen physisorption and chemisorption, hydrogen permeation and diffusion, hydrogen solution, hydrogen-metal interaction, etc.) [39]. It was pointed out that high temperatures caused negligible hydrogen trapping while low temperatures brought about low hydrogen transport, thereby limiting hydrogen effects. Intermediate temperatures allowed for maximum hydrogen-defect interactions at  $T_{HE, max}$ . Unfortunately, the mechanistic understanding of  $T_{HE, max}$  is still lacking, and the temperature effect on hydrogen diffusion and HE susceptibility needs further to be quantified and unveiled.

To conduct a practical and feasible HE assessment, the present study considered popular high-strength pipeline steel, i.e., X80 steel, for

investigation. Electrochemical hydrogen charging method was implemented to produce hydrogen environment. Hydrogen permeation and SSRT tests with hydrogen charging during straining were carried out at varying temperatures. Given the obtained hydrogen permeation parameters, mechanical behaviour and fractographic analysis, the  $T_{HE, max}$  value of X80 pipeline steel was determined, and the influence of temperature on the HE susceptibility of X80 steel was comprehensively analysed.

## 2. Experimental details

### 2.1. Material preparation

The chemical compositions of the investigated X80 steel were analysed by using energy-dispersive X-ray spectroscopy (EDS), as shown in Table 1. All element contents satisfy the requirements of API 5 L specification. The microstructures of X80 steel were characterised by a Leica DMI8 optical microscope (OM) and a Helios G4 CX scanning electron microscope (SEM) as exhibited in Fig. 1. The material was made up of massive ferrite and acicular ferrite. Electron backscattered diffraction (EBSD) map in Fig. 1b showed that the crystallographic texture was randomized, and the grain size ranged from 5  $\mu\text{m}$  to 20  $\mu\text{m}$ .

### 2.2. Hydrogen permeation tests

Hydrogen permeation tests were implemented in typical Devanathan-Stachurski cells, which consisted of a hydrogen charging cell with 0.5 mol/L  $\text{H}_2\text{SO}_4$  solution, a hydrogen oxidation cell with 0.1 mol/L NaOH solution and a sample used to separate these two cells. All samples were machined into a 30 mm  $\times$  30 mm square shape, and then were ground with SiC papers to a thickness of 1.00 mm. Subsequently, the oxidation side of samples was electroplated with Ni. A galvanostatic current density of 10 mA/cm<sup>2</sup> was used in the charging

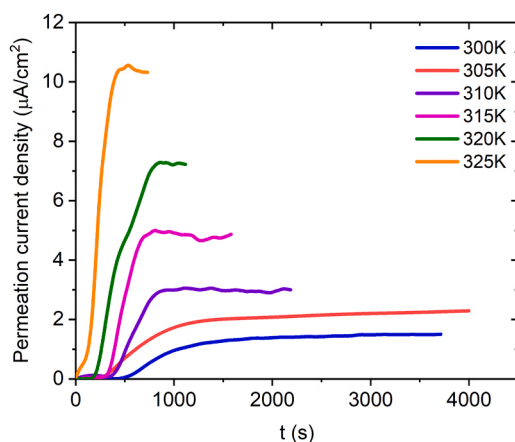


Fig. 4. Typical permeation transient at different temperatures used to determine the diffusivity.

Table 2  
Hydrogen permeation parameters at various temperatures.

Temperature (K)	$J_{HL} (\times 10^{-10}, \text{mol}/\text{m s})$	$D (\times 10^{-10}, \text{m}^2/\text{s})$	$C_0 (\text{mol}/\text{m}^3)$
300	1.27	1.91	0.66
305	1.95	2.43	0.80
310	3.11	2.61	1.19
315	5.14	3.16	1.63
320	6.82	3.73	1.83
325	10.77	5.05	2.13

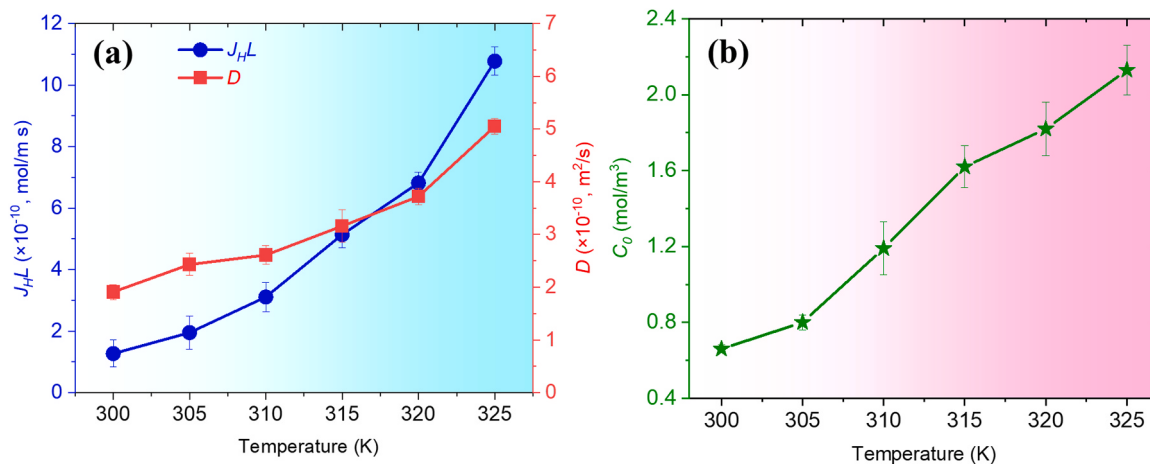


Fig. 5. The dependence of hydrogen permeation parameters on temperature.

part, while a constant potential of + 200 mV was applied on the oxidation part. As demonstrated in Fig. 2, with such a potential, the corrosion current density of Ni-plated layer of the sample was almost negligible. The background current density was shortly decreased below 0.1  $\mu\text{A}/\text{cm}^2$ , which ensured that all obtained oxidation current densities were caused by hydrogen. Hydrogen penetration parameters were determined by the oxidation current density using a Solartron 1287 potentiostat.

### 2.3. SSRT tests

The tensile samples with gauge dimensions of 30 mm  $\times$  6 mm  $\times$  2 mm (Fig. 3a) were first machined using electrical discharge machining (EDM), and were then ground to up to 1500 grit emery paper and polished to remove the oxide surface, followed by being cleaned in ethanol solution and water. SSRT tests were conducted at a tensile strain rate of  $1 \times 10^{-6}$  s $^{-1}$  using a SHIMADZU tensile tester to provide adequate time for hydrogen diffusion, absorption, and monotony in testing. As displayed in Fig. 3b, an electrochemical cell including an inner and outer chamber was designed and adapted for the straining process. The working electrode was the sample, which was mounted on a tensile machine and immersed in the inner chamber of electrochemical cell with an electrolyte (0.5 mol/L H<sub>2</sub>SO<sub>4</sub> solution with 0.2 g L $^{-1}$  CH<sub>4</sub>N<sub>2</sub>S). A piece of platinum plate was used as the counter electrode. During the entire SSRT stage, in-situ hydrogen charging method was used to continuously introduce hydrogen into the gauge part of sample at 10 mA/cm $^2$  current density. Meanwhile, a thermostatic liquid in the

outer chamber of electrochemical cell was constantly circulated to control the temperature of electrolyte. Temperature range was selected from 300 K to 325 K at an interval of 5 K [38,39]. Reference tests were carried out at 300 K in air to determine HE index. All the experiments were repeated for three times.

After SSRT tests, the specimen strain  $\varepsilon$  is defined by the ratio of the increase of the specimen gauge length  $L$  to its original gauge length  $L_0$  as  $\varepsilon = (L - L_0)/L_0 \times 100\%$ , and tensile stress  $\sigma$  is defined by the ratio of the tensile load  $F$  applied to the specimen to its original cross-sectional area  $S_0$  as  $\sigma = F/S_0$ . The reduction of cross-sectional area  $Z$  can be defined as  $Z = (S_0 - S_f)/S_0 \times 100\%$  where  $S_f$  represents cross-sectional area of samples after fracture, and HE index  $F_H$  can be defined as  $F_H = (Z_N - Z_H)/Z_N \times 100\%$  where  $Z_N$  and  $Z_H$  are the reductions of cross-sectional area in air and electrolyte, respectively.

## 3. Results

### 3.1. Hydrogen permeation parameters of X80 steel with temperature

The representative hydrogen permeation transient versus time relationships of X80 steel at various temperatures are provided in Fig. 4. The permeation current density was zero at  $t = 0$ s. It was increased prominently after a while. The period became shorter at a higher temperature, implying a less time spent by the produced hydrogen in the charging part travelling to the oxidation part. Experienced with a substantial increase, permeation current density was ultimately reached a steady state. It can be seen that both the slope of permeation transient and the magnitude of steady-state current density systematically increased when the temperature was increased, as expected from the literature results [41].

Based on the obtained steady-state current density, hydrogen permeation parameters were calculated by using a constant concentration model [42]. Assuming a sample geometry of thickness  $L$ , the hydrogen diffusion coefficient  $D$  can be analytically determined for a given  $t_{lag}$  using [40]:

$$D = \frac{L^2}{6t_{lag}} \quad (1)$$

$$i_p = 0.63i_\infty \quad (2)$$

where the lag time  $t_{lag}$  corresponds to  $i_p$  that is 63% of  $i_\infty$ , and  $i_\infty$  is the steady-state current density.

The hydrogen permeation rate  $J_H L$  is given by Ref. [43], and the subsurface hydrogen concentration  $C_0$  can be expressed by Fick's first law [42]:

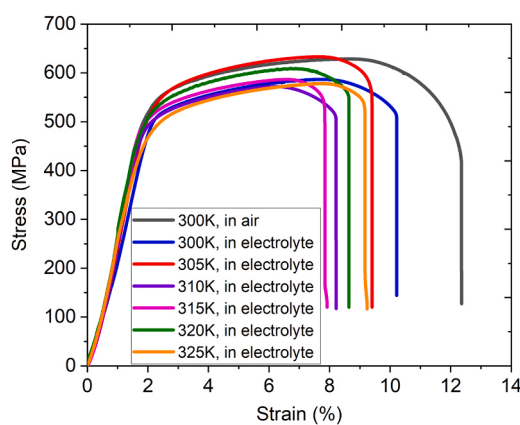


Fig. 6. Mechanical behaviour of X80 steel with in-situ hydrogen charging at various temperatures.

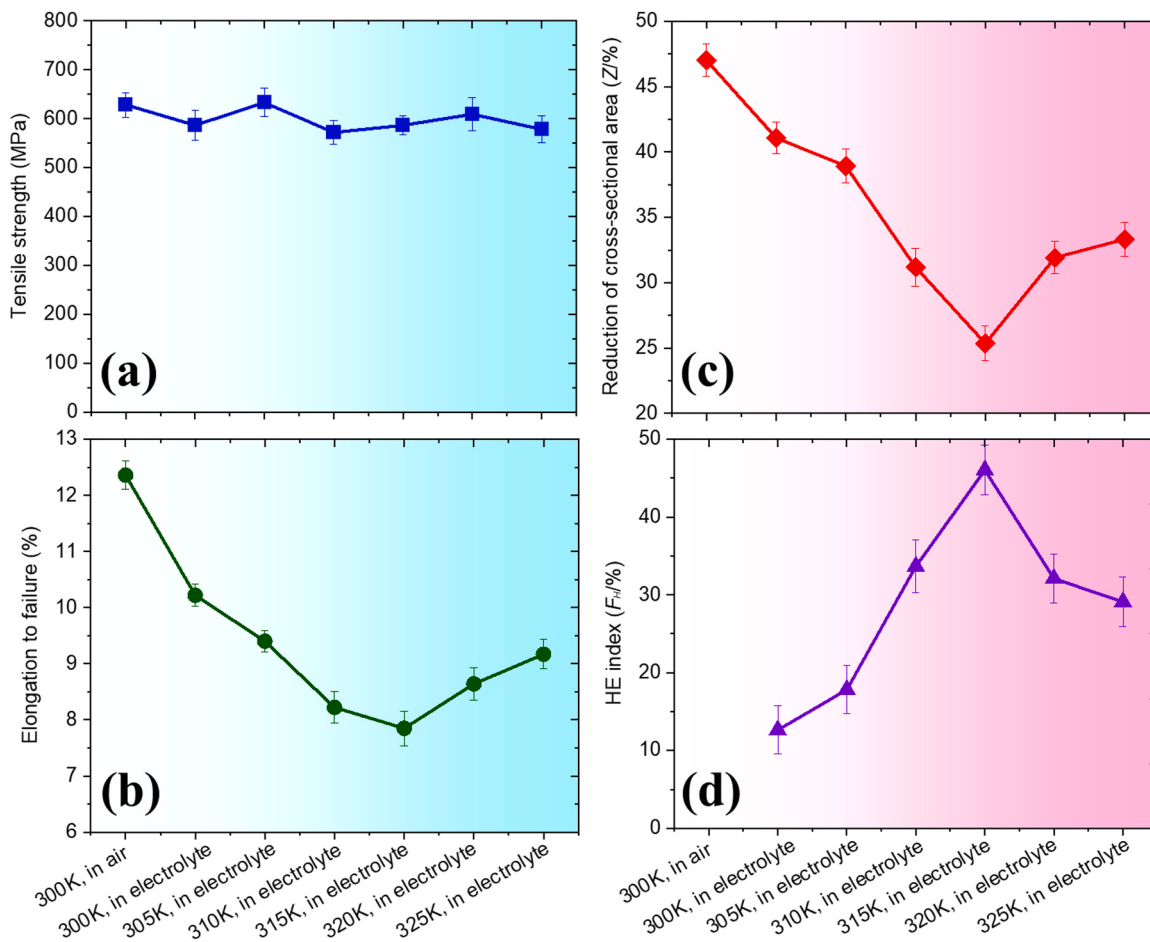


Fig. 7. The dependence of mechanical property parameters on experimental conditions.

$$J_H L = \frac{i_\infty L}{nF} \quad (3)$$

$$C_0 = \frac{J_H L}{D} \quad (4)$$

where  $J_H$  is hydrogen permeation flux,  $n$  is number of charge, and  $F$  is Faraday's constant, with a value of 96500 C/mol. Hydrogen permeation parameters derived from the permeation curves are tabulated in Table 2, and the relationships between these parameters and temperature are plotted in Fig. 5. There were some important findings including that the effective hydrogen diffusivity  $D$  was increased as the temperature increased. The positive temperature dependence implied the thermally-activated process of hydrogen diffusion jumps between neighbouring interstitial sites, consistent with previously reported results [38,41]. In addition, the calculated subsurface hydrogen concentration  $C_0$  also exhibited a systematic increase with temperature. Speculatively, it is likely that the increased temperature facilitates hydrogen charging rate, thereby yielding more hydrogen atoms at the steel subsurface.

### 3.2. Mechanical behaviour of X80 steel with temperature

SSRT tests were conducted on a 50 kN SHIMADZU tensile tester equipped with an electrochemical cell using in-situ hydrogen charging method over a temperature range of 300–325 K. Reference samples were tested in air at ambient temperature for comparison. The mechanical behaviour of tensile test samples in air at 300 K and in electrolyte at various temperatures is displayed in Fig. 6. It can be seen that there was no much difference for the mechanical behaviour in the elastic region for all samples, and there was no regular variability of the tensile

strength under various experimental conditions. The minor discrepancy in the tensile behaviour could be associated with material inhomogeneity and experimental equipment [44]. However, the stress-strain curves in Fig. 6 clearly show that the elongation to failure for hydrogen-charged samples was prominently lower than cases in air. For example, X80 sample in air showed an elongation to failure of 12.36%, and at the same temperature (300 K) the value of hydrogen-charged case was significantly reduced to 10.22%, indicating that hydrogen degradation effects were reflected on the ductility of steel. These results can be compatible to the previous literature, in which the tensile strength of pipeline steels changed negligibly, while the ductility was reduced with increasing hydrogen [38,45].

To quantitatively evaluate the susceptibility of samples to HE at various temperatures, several representative parameters including elongation to failure, reduction of cross-sectional area and HE index were calculated and shown in Fig. 7. Generally, with decreasing elongation to failure and reduction of cross-sectional area the susceptibility to HE increases. As shown in Fig. 7, elongation to failure and reduction of cross-sectional area exhibited an initial decrease with increasing temperature up to 315 K, followed by a gradual increase over the remaining range of investigated temperatures. The minima of these two parameters were reached at a temperature of 315 K, emphasising the highest HE susceptibility of X80 steel at this temperature. Based on the criteria of HE susceptibility by Kong and his coworkers [46], the material was susceptible to brittle fracture when  $F_H \geq 35\%$ ; there was a possibility of HE occurrence when  $25\% < F_H < 35\%$  and no HE failure when  $F_H \leq 25\%$ . Our results demonstrated that  $F_H$  values of X80 steel at 300 K and 305 K were 12.64% and 17.81%, respectively, implying no evident brittle failure. As the temperature increased,  $F_H$  climbed

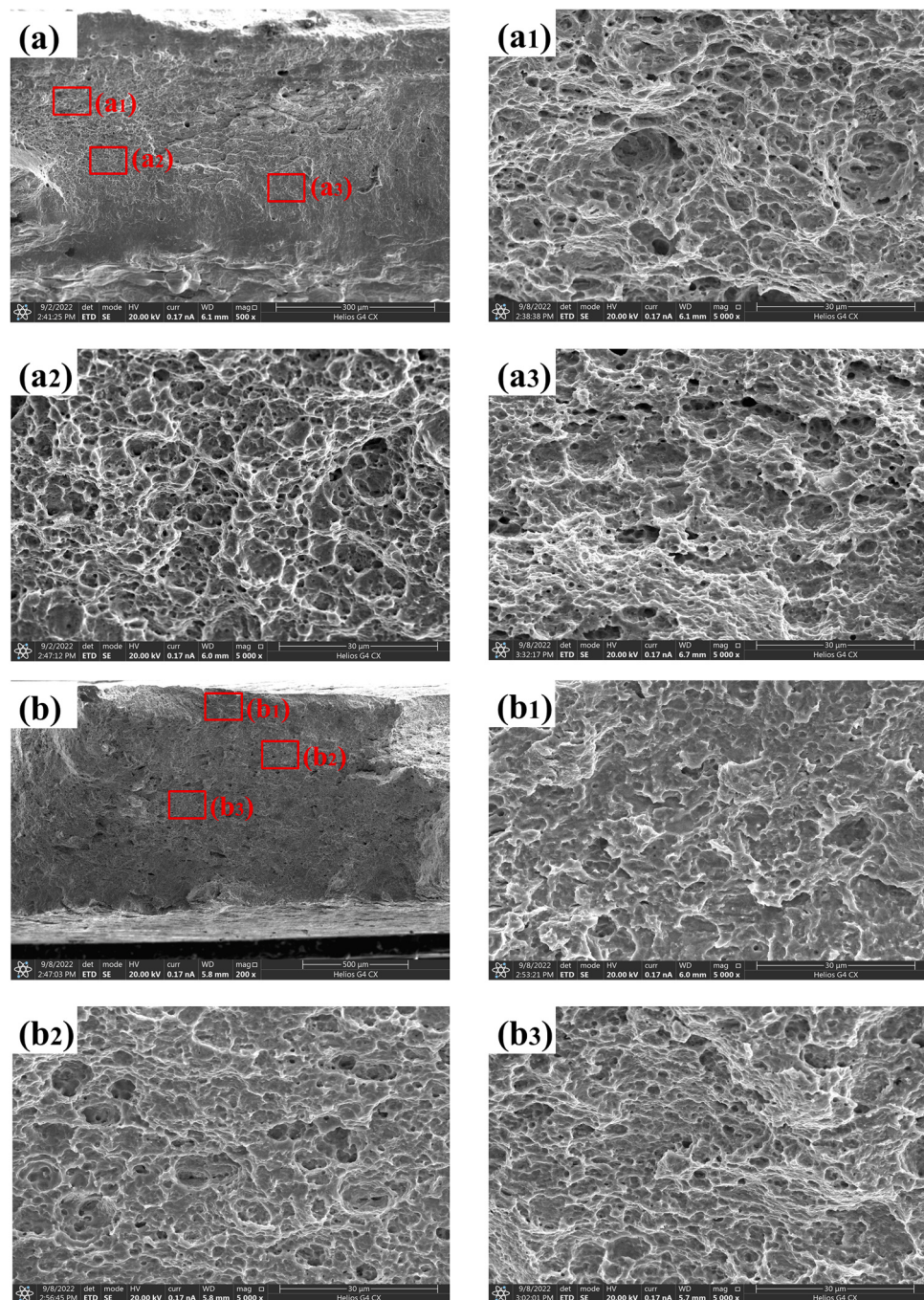


**Fig. 8.** SEM images of fracture morphologies under different experimental conditions (a) 300 K, in air and (b) 300 K, in electrolyte. (a<sub>1</sub>)-(a<sub>3</sub>) and (b<sub>1</sub>)-(b<sub>3</sub>) are high-magnification images marked in (a) and (b), respectively.

continuously and reached a maximum of 46.05% at 315 K, being indicative of that the material was prone to hydrogen-related brittle fracture. When the temperature rose to 320 K and 325 K,  $F_H$  was separately reduced to 32.10% and 29.11%, suggesting hydrogen-related embrittlement may occur. It is worthwhile noting that since the criteria of HE index was based on the empirical value, further examination of fracture morphologies would be necessary to justify HE sensitivity.

### 3.3. Fractographic analysis of X80 steel with temperature

The fracture morphologies of X80 steel in air at 300 K and in electrolyte at various temperatures are presented in Fig. 8 and Fig. 9. The

observation of fracture surfaces devoid of hydrogen (in air) typically suggested that ductile pattern dominated the failure process, as demonstrated in Fig. 8a. The magnified dimple features at different regions in Fig. 8a<sub>1</sub>-Fig. 8a<sub>3</sub> further unveiled that micro-dimples and voids mainly formed the fracture surfaces of samples. By contrast, dimples and voids in hydrogen-charged samples (300 K, in electrolyte) in Fig. 8b appeared to be shallower and smaller, which yielded flatter fracture surfaces. This phenomenon indicated a loss of ductility for X80 steel under hydrogen charging conditions, being in concordance with mechanical behaviour parameters in Fig. 7. Despite the reduction in ductility, fracture surfaces of hydrogen-charged samples still appeared a ductile pattern at 300 K.

As the temperature increased, the dimension of dimples in fracture

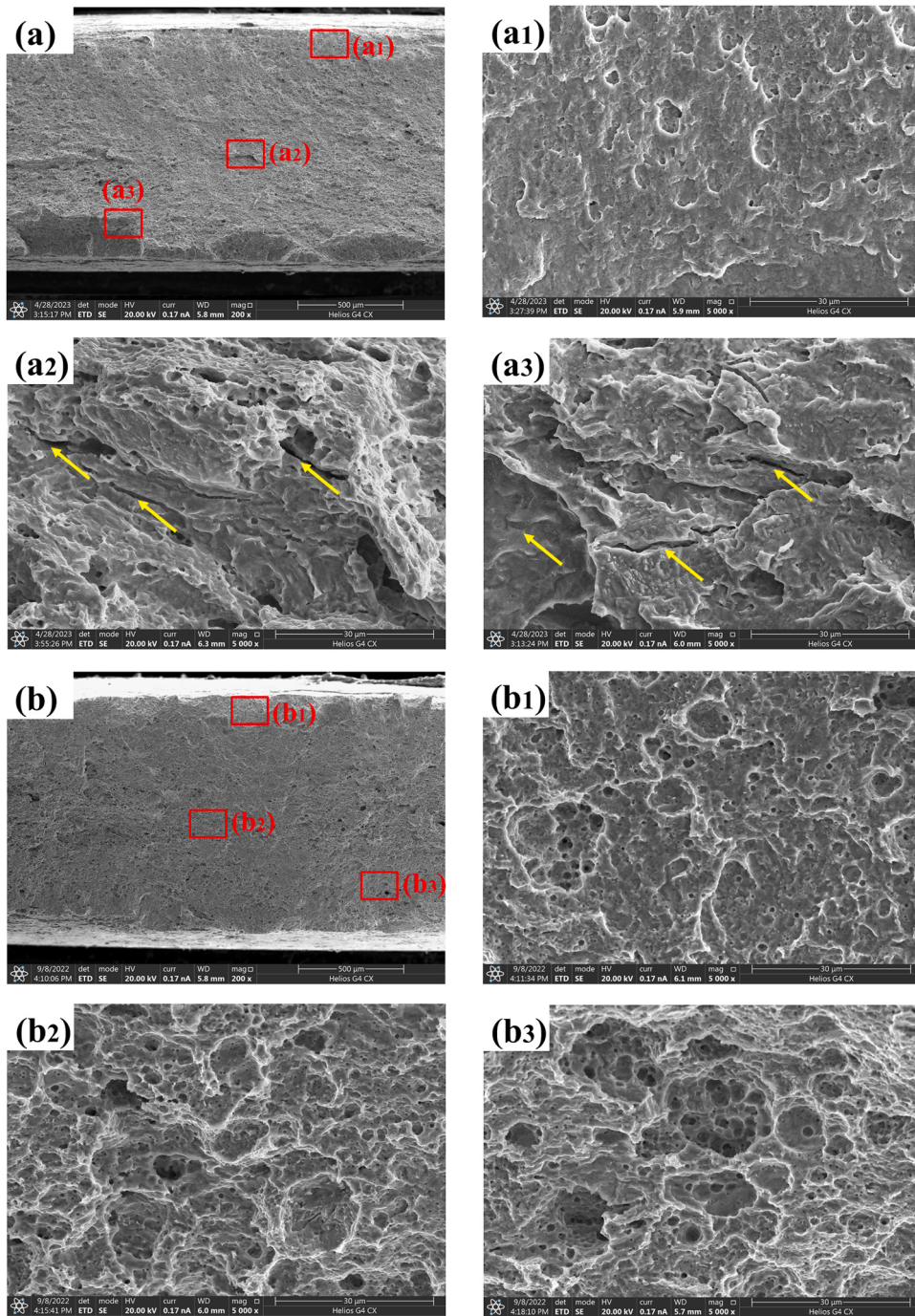


**Fig. 9.** SEM images of fracture morphologies under different experimental conditions (a) 315 K, in electrolyte and (b) 325 K, in electrolyte. (a<sub>1</sub>)-(a<sub>3</sub>) and (b<sub>1</sub>)-(b<sub>3</sub>) are high-magnification images marked in (a) and (b), respectively.

surfaces was further decreased, and the number of ductile features was on the decline. At a temperature of 315 K, the fracture surface was composed of obvious brittle features, as shown in Fig. 9a. Specifically, typical dimples almost disappeared; instead, brittle fracture characteristics such as secondary cracks and quasi-cleavage planes occurred. These observations can be compatible with previous studies of pipeline steels [5,38,45,47]. For example, Zhang et al. [5] compared HE susceptibility of subsea pipeline steels under cathodic protection, and found similar fracture surfaces of X80 and X100 steels characterised by secondary cracks and quasi-cleavage planes. When the temperature continued to rise, it is worthwhile noting that fracture surfaces appeared in a ductile pattern again, evidenced by a number of dimples and voids as shown in Fig. 9b<sub>1</sub>-Fig. 9b<sub>3</sub>.

From the above fractographic analysis, it can be concluded that the ductility declined as the temperature increased to 315 K, then increased with further temperature. At the temperature of 315 K, brittle patterns such as quasi-cleavage planes and cracks occurred, suggesting that HE susceptibility was the highest and in line with the HE index in Fig. 7.

#### 4. Discussion

The temperature dependence of hydrogen diffusion was studied in the present study by permeation experiments. Theoretically, diffusion coefficient  $D$  as a function of temperature  $T$  follows the Arrhenius equation:

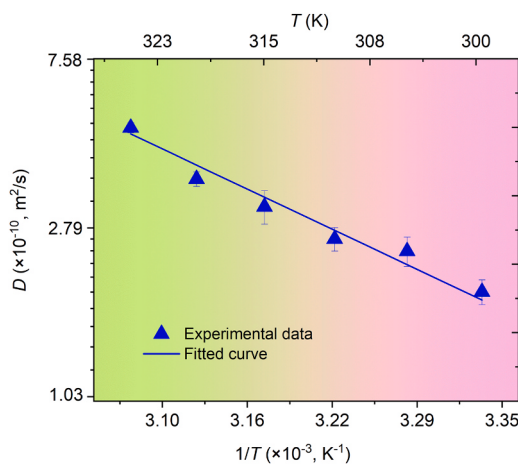


Fig. 10. Hydrogen diffusivity as a function of the inverse of temperature.

$$D = D_0 \exp\left(\frac{-E_a}{RT}\right) \quad (5)$$

where  $D_0$  represents the pre-exponential factor,  $E_a$  is the activation energy of hydrogen atom diffusion, and  $R$  is the ideal gas state constant. Using a log-linear plot, the obtained hydrogen diffusivity as a function of the inverse of temperature are shown in Fig. 10. As expected,  $\log(D_0)$  can be determined as the independent term of linear regression, and  $E_a$  can be calculated by  $R$  multiplied by the slope. The fitted values of  $D_0$  and  $E_a$  are  $6.51 \times 10^{-5} \text{ m}^2/\text{s}$  and  $31.90 \text{ kJ/mol}$ , respectively.

Note that diffusion coefficients obtained from the current experiments are distinct from the reported values in the literature for X80 steel. For example, Cui et al. [48] performed a thorough analysis of hydrogen diffusion with temperature, reporting that typical  $D_0$  and  $E_a$  values were  $3.55 \times 10^{-3} \text{ m}^2/\text{s}$  and  $41.77 \text{ kJ/mol}$  for Nb-free-X80 steel, and  $5.64 \times 10^{-4} \text{ m}^2/\text{s}$  and  $39.56 \text{ kJ/mol}$  for 0.055 wt% Nb-X80 steel. As such, it was speculated that the Nb microalloying element was likely responsible for the low observed diffusivity. The higher Nb weight percentage (0.07 wt%) of samples in the current study can induce NbC precipitates and coherent interfaces [49], which acted as strong hydrogen traps, thereby increasing the difficulty of hydrogen diffusion.

Regarding the mechanical properties and fracture morphologies in Fig. 6–Fig. 9, it was clear that hydrogen-induced embrittlement susceptibility was strongly dependent on the temperature for X80 steel, giving rise to a specific temperature  $T_{HE, max}$  of 315 K. This threshold lay well within the experimental data regime between 175 and 345 K for iron, carbon steels, heat-treatable steels, and high alloyed body-centred cubic (BCC) steels suggested by Michler et al., who performed a thorough analysis of the existing literature about the influence of temperature upon hydrogen effects in structural materials [37]. Given the complexity of temperature-dependent steps in the hydrogen reaction chain, a sophisticated interpretation of scenarios behind  $T_{HE, max}$  was not provided. Bergmann et al. [50] developed a semi quantitative model based on trapping coverage at the crack tip in gaseous hydrogen experiments to elucidate the temperature dependence, but doubts were thrown on whether some steps of the hydrogen reaction chain were primary for determining  $T_{HE, max}$ . For example, hydrogen reaction processes such as physical adsorption and dissociative chemical adsorption were only relevant for gaseous hydrogen tests. If these steps directly controlled  $T_{HE, max}$ , the ductility minimum would not exist for electrochemical hydrogen charging tests, which was not the case.

Borchers et al. [51] and Wu et al. [52] suggested the temperature-dependent mechanisms being associated with hydrogen-defect interactions, which might play a critical role in governing  $T_{HE, max}$ . Unfortunately, current experimental techniques cannot characterize these interactions involving in nanoscale hydrogen distribution around lattice defects. However, modern simulation tools might

provide nanoscale details of hydrogen interactions required to illuminate temperature effects [37,38,53]. For example, Xing et al. [53] studied the equilibrium hydrogen concentration at the microcrack using molecular dynamics (MD) simulations. They found that the hydrogen movement ( $V$ ), bulk hydrogen concentration and the amount of hydrogen atoms ( $N$ ) required to saturate the stress-concentrated zone around the crack tip were increased with increasing the temperature, and there was a temperature threshold of  $N/V$  to maximize the hydrogen embrittlement. As such, further studies of hydrogen-defect interactions using simulation tools are required to provide an atomistic-level explanation of the temperature-dependent HE in structural materials.

## 5. Conclusions

The hydrogen diffusion and hydrogen-induced embrittlement susceptibility for X80 pipeline steel at various temperatures were measured by means of both electrochemical hydrogen permeation tests and SSRT tests. Furthermore, a thorough analysis of fracture morphologies was performed to interpret the prevalent mechanisms behind  $T_{HE, max}$ . According to these results, the following conclusions were made:

- Hydrogen diffusion coefficient and subsurface hydrogen concentration, determined by the hydrogen permeation tests, exhibited a systematic increase with increasing temperature over the range of 300–325 K. The hydrogen diffusivity as a function of temperature relationships fitted well with the Arrhenius analysis.
- Elongation to failure and reduction of cross-sectional area of X80 steel under electrochemical hydrogen charging environment showed a minimum while HE index exhibited a maximum at a temperature of 315 K. These results suggested the temperature threshold of HE being  $T_{HE, max} = 315 \text{ K}$ .
- Fracture morphologies presented ductile features composed of dimples and voids at various temperatures except the case of 315 K, where brittle patterns featured by quasi-cleavage planes and secondary cracks were observed. Such ductile-to-brittle transition was in excellent agreement with HE index.
- The comprehensive investigation of embrittlement susceptibility of structural materials at various temperatures would provide mechanistic insights into understanding temperature effects on hydrogen-related engineering material applications.

## CRediT authorship contribution statement

**Jiaqing Li:** Methodology, Software, Writing – original draft preparation. **Ziyue Wu:** Investigation, Validation. **Lijie Zhu:** Investigation, Validation. **Zhuwu Zhang:** Methodology, Project administration. **Lin Teng:** Conceptualization, Funding acquisition. **Liang Zhang:** Software, Visualization, Writing – reviewing and editing. **Cheng Lu:** Supervision, Funding acquisition. **Rui Wang:** Writing – reviewing and editing. **Che Zhang:** Visualization, Investigation.

## Declaration of Competing Interest

The authors declare that they have no known competing financial interests or personal relationships that could have appeared to influence the work reported in this paper.

## Data availability

Data will be made available on request.

## Acknowledgements

This study was financially supported by the National Natural Science Foundation of China (No. 52205145), Research Program for Young and Middle-Aged Teachers of Fujian Province (No. JAT210038; No.

JAT220008), Talent Program of Fuzhou University (No. XRC-22024), and Qingyuan Innovation Laboratory Testing Fund of Precious Apparatus (No. QYT2023035).

## References

- [1] M. Asadipoor, A. Pourkamali Anaraki, J. Kadkhodapour, S.M.H. Sharifi, A. Barnoush, Macro- and microscale investigations of hydrogen embrittlement in X70 pipeline steel by in-situ and ex-situ hydrogen charging tensile tests and in-situ electrochemical micro-cantilever bending test, *Mater. Sci. Eng. A* 772 (2020), 138762.
- [2] G. Domizzi, G. Anteri, J. Ovejero-Garcia, Influence of sulphur content and inclusion distribution on the hydrogen induced blister cracking in pressure vessel and pipeline steels, *Corros. Sci.* 43 (2) (2011) 325–339.
- [3] C.F. Dong, Z.Y. Liu, X.G. Li, Y.F. Cheng, Effects of hydrogen-charging on the susceptibility of X100 pipeline steel to hydrogen-induced cracking, *Int. J. Hydrog. Energy* 34 (24) (2009) 9879–9884.
- [4] B. Beidokhti, A. Dolati, A.H. Koukabi, Effects of alloying elements and microstructure on the susceptibility of the welded HSLA steel to hydrogen-induced cracking and sulfide stress cracking, *Mater. Sci. Eng. A* 507 (1–2) (2009) 167–173.
- [5] T. Zhang, W. Zhao, T. Li, Y. Zhao, Q. Deng, Y. Wang, W. Jiang, Comparison of hydrogen embrittlement susceptibility of three cathodic protected subsea pipeline steels from a point of view of hydrogen permeation, *Corros. Sci.* 131 (2018) 104–115.
- [6] W. Zhao, T. Zhang, Y. Zhao, J. Sun, Y. Wang, Hydrogen permeation and embrittlement susceptibility of X80 welded joint under high-pressure coal gas environment, *Corros. Sci.* 111 (2016) 84–97.
- [7] J.Q. Tang, J.M. Gong, X.C. Zhang, S.T. Tu, Comparison on the cracking susceptibility of different low alloy steel weldments exposed to the environment containing wet H<sub>2</sub>S, *Eng. Fail. Anal.* 13 (7) (2006) 1057–1064.
- [8] N. Nanninga, J. Grochowski, L. Heldt, K. Rundman, Role of microstructure, composition and hardness in resisting hydrogen embrittlement of fastener grade steels, *Corros. Sci.* 52 (4) (2010) 1237–1246.
- [9] W.H. Johnson, On some remarkable changes produced in iron and steel by the action of hydrogen and acids, *Nature* 11 (1875) 393.
- [10] A.R. Troiano, The role of hydrogen and other interstitials in the mechanical behavior of metals, *Trans. Asm.* 52 (1960) 54–80.
- [11] D.H. Lassila, H.K. Birnbaum, The effect of diffusive hydrogen segregation on fracture of polycrystalline nickel, *Acta Met.* 34 (1986) 1237–1243.
- [12] J. Li, C. Lu, L. Pei, C. Zhang, R. Wang, Atomistic investigation of hydrogen induced decohesion of Ni grain boundaries, *Mech. Mater.* 150 (2020), 103586.
- [13] J. Li, C. Lu, L. Pei, C. Zhang, K. Tieu, Influence of solute hydrogen on the interaction of screw dislocations with vicinal twin boundaries in nickel, *Scr. Mater.* 173 (2019) 115–119.
- [14] H.K. Birnbaum, P. Sofronis, Hydrogen-enhanced localized plasticity—a mechanism for hydrogen-related fracture, *Mater. Sci. Eng. A* 176 (1994) 191–202.
- [15] I.M. Robertson, The effect of hydrogen on dislocation dynamics, *Eng. Fract. Mech.* 68 (2001) 671–692.
- [16] M.B. Djukic, G.M. Bakic, V. Sijacki Zeravcic, A. Sedmak, B. Rajcic, The synergistic action and interplay of hydrogen embrittlement mechanisms in steels and iron: Localized plasticity and decohesion, *Eng. Fract. Mech.* 216 (2019), 106528.
- [17] M.L. Martin, M. Dadfarnia, A. Nagao, S. Wang, P. Sofronis, Enumeration of the hydrogen-enhanced localized plasticity mechanism for hydrogen embrittlement in structural materials, *Acta Mater.* 165 (2019) 734–750.
- [18] S. Wang, A. Nagao, P. Sofronis, I.M. Robertson, Hydrogen-modified dislocation structures in a cyclically deformed ferrite-pearlitic low carbon steel, *Acta Mater.* 144 (2018) 164–176.
- [19] I.M. Robertson, P. Sofronis, A. Nagao, M.L. Martin, S. Wang, D.W. Gross, K. E. Nygren, Hydrogen embrittlement understood, *Metall. Mater. Trans. A* 46 (6) (2015) 2323–2341.
- [20] Y. Deng, A. Barnoush, Hydrogen embrittlement revealed via novel in situ fracture experiments using notched micro-cantilever specimens, *Acta Mater.* 142 (2018) 236–247.
- [21] D. Xie, S. Li, M. Li, Z. Wang, P. Gumbusch, J. Sun, E. Ma, J. Li, Z. Shan, Hydrogenated vacancies lock dislocations in aluminium, *Nat. Commun.* 7 (2016) 13341.
- [22] R. Silverstein, D. Eliezer, E. Tal-Gutelmacher, Hydrogen trapping in alloys studied by thermal desorption spectrometry, *J. Alloy. Comp.* 747 (2018) 511–522.
- [23] A. Laureys, E. Van den Eeckhout, R. Petrov, K. Verbeken, Effect of deformation and charging conditions on crack and blister formation during electrochemical hydrogen charging, *Acta Mater.* 127 (2017) 192–202.
- [24] J. Venezuela, C. Tapia-Bastidas, Q. Zhou, T. Depover, K. Verbeken, E. Gray, A. Atrens, Determination of the equivalent hydrogen fugacity during electrochemical charging of 3.5 NiCrMoV steel, *Corros. Sci.* 132 (2018) 90–106.
- [25] Q. Liu, J. Venezuela, M. Zhang, Q. Zhou, A. Atrens, Hydrogen trapping in some advanced high strength steels, *Corros. Sci.* 111 (2016) 770–785.
- [26] J. Yamabe, M. Yoshikawa, H. Matsunaga, S. Matsuoka, Hydrogen trapping and fatigue crack growth property of low-carbon steel in hydrogen-gas environment, *Int. J. Fatigue* 102 (2017) 202–213.
- [27] J. Yamabe, O. Takakuwa, H. Matsunaga, H. Itoga, S. Matsuoka, Hydrogen diffusivity and tensile-ductility loss of solution-treated austenitic stainless steels with external and internal hydrogen, *Int. J. Hydrog. Energy* 42 (18) (2017) 13289–13299.
- [28] B.P. Somerd़ay, P. Sofronis, K.A. Nibur, C. San Marchi, R. Kirchheim, Elucidating the variables affecting accelerated fatigue crack growth of steels in hydrogen gas with low oxygen concentrations, *Acta Mater.* 61 (16) (2013) 6153–6170.
- [29] Y. Ogawa, D. Birenis, H. Matsunaga, A. Thøgersen, Ø. Prytz, O. Takakuwa, J. Yamabe, Multi-scale observation of hydrogen-induced, localized plastic deformation in fatigue-crack propagation in a pure iron, *Scr. Mater.* 140 (2017) 13–17.
- [30] T. Depover, E. Wallaert, K. Verbeken, Fractographic analysis of the role of hydrogen diffusion on the hydrogen embrittlement susceptibility of DP steel, *Mater. Sci. Eng. A* 649 (2016) 201–208.
- [31] D. Sun, G. Han, S. Vaadee, S. Fukuyama, K. Yokogawa, Tensile behaviour of type 304 austenitic stainless steels in hydrogen atmosphere at low temperatures, *Mater. Sci. Technol.* 17 (2001) 302–308.
- [32] L. Zhang, M. Wen, M. Imade, S. Fukuyama, K. Yokogawa, Effect of nickel equivalent on hydrogen gas embrittlement of austenitic stainless steels based on type 316 at low temperatures, *Acta Mater.* 56 (2008) 3414–3421.
- [33] G. Odemer, E. Andrieu, C. Blanc, J.-M. Cloue, F. Galliano, Effect of Metallurgical State and Temperature on the Hydrogen Embrittlement Susceptibility of Alloy 718. In Proceedings of the International Hydrogen Conference (IHC 2012): Hydrogen-Materials Interactions, Jackson Lake Lodge, WY, USA, 9–12 September 2014; 421–430.
- [34] M. Imade, L. Zhang, T. Iijima, S. Fukuyama, K. Yokogawa, Effect of Temperature on Internal Reversible Hydrogen Embrittlement of SUH660 Iron-Based Superalloy and Austenitic Stainless Steels at Low Temperature, *J. Jpn. Inst. Met.* 73 (2009) 245–250.
- [35] L. Zhang, M. Wen, S. Fukuyama, K. Yokogawa, Effect of temperature on hydrogen environment embrittlement of carbon steels at low temperatures, *J. Jpn. Inst. Met.* 67 (2003) 460–463.
- [36] H. Matsunaga, M. Yoshikawa, R. Kondo, J. Yamabe, S. Matsuoka, Slow strain rate tensile and fatigue properties of Cr–Mo and carbon steels in a 115 MPa hydrogen gas atmosphere, *Int. J. Hydrog. Energy* 40 (2015) 5739–5748.
- [37] T. Michler, F. Schweizer, K. Wackermann, Review on the influence of temperature upon hydrogen effects in structural alloys, *Metals* 11 (2021) 423.
- [38] X. Xing, R. Cheng, G. Cui, J. Liu, J. Gou, C. Yang, Z. Li, F. Yang, Quantification of the temperature threshold of hydrogen embrittlement in X90 pipeline steel, *Mater. Sci. Eng. A* 800 (2021), 140118.
- [39] C. Borchers, T. Michler, A. Pundt, Effect of hydrogen on the mechanical properties of stainless steels, *Adv. Eng. Mater.* 10 (2008) 11–23.
- [40] M.A.V. Devanathan, Z. Stachurski, The adsorption and diffusion of electrolytic hydrogen in palladium, *Proc. R. Soc.* 270 (1962) 90–102.
- [41] A. Zafra, Z. Harris, C. Sun, E. Martínez-Pañeda, Comparison of hydrogen diffusivities measured by electrochemical permeation and temperature-programmed desorption in cold-rolled pure iron, *J. Nat. Gas. Sci. Eng.* 98 (2022), 104365.
- [42] Y.F. Cheng, Analysis of electrochemical hydrogen permeation through X-65 pipeline steel and its implications on pipeline stress corrosion cracking, *Int. J. Hydrog. Energy* 32 (2007) 1269–1276.
- [43] S.H. Wang, Hydrogen permeation in a submerged arc weldment of TMCP steel, *Mater. Chem. Phys.* 77 (2003) 447–454.
- [44] N.E. Nanninga, Y.S. Levy, E.S. Drexlter, R.T. Condon, A.E. Stevenson, A.J. Slifka, Comparison of hydrogen embrittlement in three pipeline steels in high-pressure gaseous hydrogen environments, *Corros. Sci.* 59 (2012) 1–9.
- [45] I. Moro, L. Briottet, P. Lemoine, E. Andrieu, C. Blanc, G. Odemer, Hydrogen embrittlement susceptibility of a high strength steel X80, *Mater. Sci. Eng. A* 527 (2010) 7252–7260.
- [46] D. Kong, Y. Wu, D. Long, Stress corrosion of X80 pipeline steel welded joints by slow strain test in NACE H<sub>2</sub>S solutions, *J. Iron Steel Res. Int* 20 (2013) 40–46.
- [47] B. Meng, C. Gu, L. Zhang, C. Zhou, X. Li, Y. Zhao, J. Zheng, X. Chen, Y. Han, Hydrogen effects on X80 pipeline steel in high-pressure natural gas/hydrogen mixtures, *Int. J. Hydrog. Energy* 42 (2017) 7404–7412.
- [48] Q. Cui, J. Wu, D. Xie, X. Wu, Y. Huang, X. Li, Effect of nanosized NbC precipitates on hydrogen diffusion in X80 pipeline steel, *Materials* 10 (2017) 721.
- [49] Y.F. Cheng, Analysis of electrochemical hydrogen permeation through X-65 pipeline steel and its implications on pipeline stress corrosion cracking, *Int. J. Hydrog. Energy* 32 (2007) 1269–1276.
- [50] G. Bergmann, Untersuchungen zur Wasserstoffversprödung von NiAl, TiAl und CMSX-6. VDI Verlag; 1995.
- [51] C. Borchers, T. Michler, A. Pundt, Effect of hydrogen on the mechanical properties of stainless steels, *Adv. Eng. Mater.* 10 (2008) 11–23.
- [52] X. Wu, I. Kim, Effects of strain rate and temperature on tensile behavior of hydrogen-charged SA508 Cl.3 pressure vessel steel, *Mater. Sci. Eng. A* 348 (2003) 309–318.
- [53] X. Xing, J. Zhou, S. Zhang, H. Zhang, Z. Li, Z. Li, Quantification of temperature dependence of hydrogen embrittlement in pipeline steel, *Materials* 12 (4) (2019) 585.